

Strain-Induced Ferromagnetism in Antiferromagnetic LuMnO₃ Thin Films

J. S. White,^{1,2} M. Bator,³ Y. Hu,³ H. Luetkens,⁴ J. Stahn,¹ S. Capelli,⁵ S. Das,⁶ M. Döbeli,⁷ Th. Lippert,³ V. K. Malik,⁶ J. Martynczuk,⁸ A. Wokaun,³ M. Kenzelmann,⁹ Ch. Niedermayer,¹ and C. W. Schneider^{3,*}

¹Laboratory for Neutron Scattering, Paul Scherrer Institut, CH-5232 Villigen, Switzerland

²Laboratory for Quantum Magnetism, Ecole Polytechnique Fédérale de Lausanne, CH-1015 Lausanne, Switzerland

³General Energy Research Department, Paul Scherrer Institut, CH-5232 Villigen, Switzerland

⁴Laboratory for Muon-Spin Spectroscopy, Paul Scherrer Institut, CH-5232 Villigen, Switzerland

⁵Institut Laue-Langevin, 6 rue Jules Horowitz, 38042 Grenoble, France

⁶Department of Physics and Fribourg Centre for Nanomaterials, University of Fribourg, CH-1700 Fribourg, Switzerland

⁷Labor für Ionenstrahlphysik, ETH Zürich, CH-8093 Zürich, Switzerland

⁸Electron Microscopy Center of ETH Zürich (EMEZ), ETH Zürich, CH-8093 Zürich, Switzerland

⁹Laboratory for Developments and Methods, Paul Scherrer Institut, CH-5232 Villigen, Switzerland

Single phase and strained LuMnO₃ thin films are discovered to display coexisting ferromagnetic and antiferromagnetic orders. A large moment ferromagnetism ($\approx 1\mu_B$), which is absent in bulk samples, is shown to display a magnetic moment distribution that is peaked at the highly strained substrate-film interface. We further show that the strain-induced ferromagnetism and the antiferromagnetic order are coupled via an exchange field, therefore demonstrating strained rare-earth manganite thin films as promising candidate systems for new multifunctional devices.

Interfaces of transition metal oxides are a fertile ground for new physics, often showing novel electronic and magnetic properties that do not exist in the bulk of the materials [1]. Most notably, interfaces of insulating perovskite layers were shown to be conducting [2–4], superconducting [4], and ferromagnetic (FM) [5–7]. Domain boundaries demonstrate equally diverse and fascinating emergent phenomena and were shown to be conductive [8] or ferroelectric [9]. While the mechanisms of these novel properties are not completely understood, their possible origins include charge transfer, spin-orbital reconstruction, and strain or strain gradient effects [1,10].

The engineering of multifunctional transition metal oxide interfaces offers vast potential for new discoveries, while simultaneously posing considerable experimental and theoretical challenges [11,12]. One little-explored direction concerns the interfacial properties of the magnetoelectric multiferroics. Classic examples include orthorhombic (o-) REMnO₃ (RE = Tb, Lu, Y), in which a symmetry-breaking magnetic transition causes the direct coupling of antiferromagnetic (AFM) and ferroelectric properties [13,14]. Surprisingly, studies on both o-TbMnO₃ and o-YMnO₃ thin films report the existence of a FM magnetization loop [15,16]. It is proposed that the ferromagnetism may arise from domain boundaries [17] or from a uniform canting of an AFM spin structure [18].

To answer the intriguing question regarding the origin of an insulating FM phase in an otherwise AFM system, here we present a combined study of both structural and magnetic properties in highly strained LuMnO₃ thin films grown on nonmagnetic YAlO₃ substrates. By both Rutherford backscattering and transmission electron

microscopy, we identify distinct structural properties for differently strained regions in the films. The magnetic measurements reveal the films to display a coexisting FM and AFM phase, in contrast to the bulk state which is solely a stable *E*-type antiferromagnet [19–21]. Crucially, we show that the FM magnetization in our films exists mostly close to the film-substrate interface. This is a region where the effects of lattice strain on the crystal properties is largest, and so the lattice strain is identified as the key ingredient for ferromagnetism. We also show the existence of an exchange field between the FM and AFM orders in the films, and which paves the way for studies that are relevant for applications.

Epitaxial thin films of o-LuMnO₃ (LMO) were grown on (110) oriented YAlO₃ (YAO) [22], with the [1 -1 0] and [001] axes parallel to the substrate surface and the [110] axis out of plane. Full details of the film synthesis are given in Ref. [23]. By x-ray diffraction (XRD) the films are shown to be single phase, untwinned, and of single crystalline quality [23,24]. Rocking scans of the (110) film peaks along the growth direction display a FWHM that is typically $\leq 0.06^\circ$. For thicker films up to 200 nm, the FWHM remains $< 0.10^\circ$. At the out-of-plane (110) film peak, Laue oscillations are observed indicating well-aligned film lattice planes.

Table I contains film lattice parameters determined by both XRD and neutron measurements. The parameters extracted by both techniques are compatible with the orthorhombic *Pbnm* space group. However, a better match for the XRD data is obtained when including a small monoclinic distortion in particular for the thinner films measured [23,24]. The neutron diffraction experiments

TABLE I. The lattice constants of both the YAIO_3 substrate and the LuMnO_3 (LMO) films determined by both x rays and neutrons. Values for bulk LMO are taken from Ref. [20]. All values are given for $T = 298$ K and the $Pbnm$ space group.

	YAIO_3 substrate	LMO (x rays)	LMO (neutrons)	LMO (bulk)
a (\AA)	5.18	5.21	5.19	5.20
b (\AA)	5.31	5.73	5.76	5.79
c (\AA)	7.35	7.36	7.34	7.30

were insensitive to the monoclinic distortion for the films measured with a thickness of around 90 nm; its inclusion in the refinement of a set of structural Bragg peaks gave no improvement compared with that done in the $Pbnm$ space group. Compared with bulk o-LMO, on average the film is stretched along the c axis and compressively strained along the $[110]$ direction [Fig. 1(a)]. This strain pattern is typical for LMO films grown on YAO and where thinner films show more pronounced strain effects than thicker films ($t \geq 200$ nm) [24]. Figure 1(a) illustrates how strain leads to the monoclinic distortion that lowers the crystal symmetry at the interface [24]. Furthermore, the strain along the $[001]$ and $[1 - 10]$ directions modifies the anisotropy of the MnO_6 bonding and Mn orbital ordering, and the severe distortion of the MnO_6 octahedron [25] is expected to influence the magnetic properties of these thin films.

The crystallinity of the LMO thin films was studied using both channeling Rutherford backscattering (c-RBS) and high resolution transmission electron microscopy (HRTEM). c-RBS measurements were done on an ≈ 56 nm thick film and using a 2 MeV ^4He ion beam aligned with the film surface normal in order to study the energy, and hence, the depth dependence of the ion channeling [26]. The part of the spectrum due to Lu ions in the sample [Fig. 1(b)] shows a clear dip in backscattering yield between two regions of higher yield. The dip reflects increased ion channeling, which evidences a coherent and highly crystalline central portion of the film. The two higher yield regions show reduced ion channeling in the vicinity of the film surface (higher channel number) and substrate-film interface (lower channel number), and may be caused by strain, incoherency in the crystal lattice, and crystal defects. By simulating the c-RBS spectrum, we identify three main film regions—interface, coherent, and surface—with approximate thicknesses 9, 40, and 6 nm. However, the boundaries between these regions are likely not sharply defined. Nonetheless, while reduced channeling at the surface is expected due to both random atom distribution and disorder, the reduction close to the LMO-YAO interface indicates the existence of a broader region of crystal imperfections.

HRTEM measurements were conducted using an FEI Tecnai F30 TEM (300 keV) [23]. Figure 1(c) shows a HRTEM image of the interface region along the $[001]$

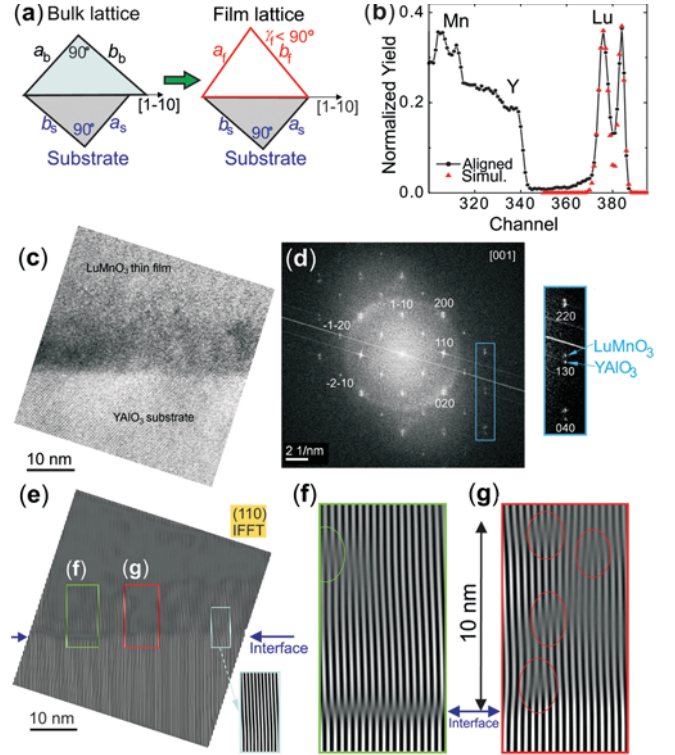


FIG. 1 (color online). (a) Sketch of the substrate-induced rhomboidal distortion of the \mathbf{ab} -plane in thin film LMO, as compared with the undistorted lattice of bulk o-LMO. (b) The c-RBS spectrum of the LMO thin film on the YAO substrate, focusing on the contribution due to Lu. Black dots represent the raw data. The red triangles are the simulation. (c) A HRTEM image of a LMO thin film on the YAO substrate at 390 kx magnification. (d) The corresponding diffraction image of panel (c). (e) The reconstructed image of the (110) lattice planes after an inverse FFT. The inset blue window highlights a region of coherently strained film-substrate lattice planes. (f) and (g) show magnified images of the green and red regions in panel (e). Ovals highlight crystal defects.

zone axis of an ≈ 56 nm thick LMO film. The corresponding diffraction image of Fig. 1(c) is shown in Fig. 1(d), and it is found that the positions of the film diffraction spots are located vertically above those of the substrate (inset, Fig. 1(d) and Fig. 2 of Supplemental Material [23]). These spot locations are different from those expected for bulk o-LMO on the YAIO_3 substrate [23]. This shows the illuminated part of the film to contain lattice planes that are both epitaxially and compressively strained to match the underlying substrate lattice along the in-plane $[110]$ direction. The diffraction image also shows weak intensity haloes; these evidence a degree of film amorphization induced by the focused ion beam technique used to prepare the films for the HRTEM [23]. Since the amorphization occurs mostly at distances > 10 nm from the direct interface, we focus on the as-grown film crystallinity at shorter distances.

To study the film strain close to the LMO-YAO interface, images of a strain field contrast are reconstructed by an

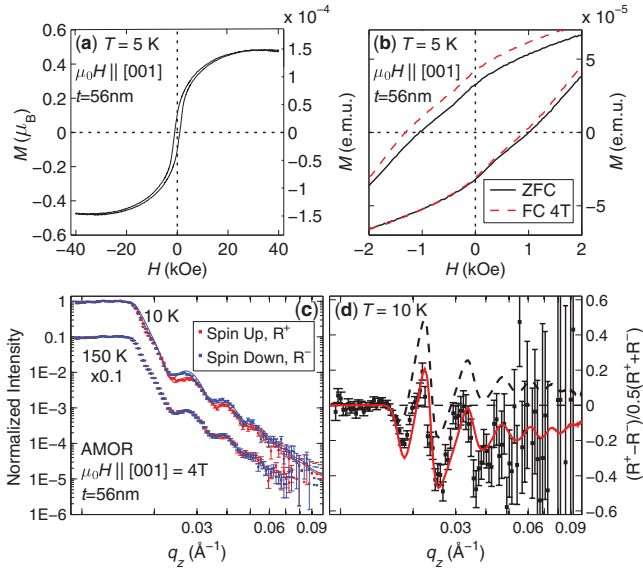


FIG. 2 (color online). (a) $M(H)$ loop for the LMO sample ($t \approx 56$ nm) after a zero-field cool (ZFC) to 5 K with $\mu_0 H \parallel (001)$. (b) The same ZFC $M(H)$ loop as in panel (a) (black) and a loop measured after field cooling the sample to 5 K in 4 T (red). (c) Intensities from PNR measurements as a function of q_z at 10 and 150 K. The latter is multiplied by 0.1 for clarity. (d) The normalized spin-up and -down ratio at 10 K. The red (black) lines describe fits to the data using a Gaussian profile for the magnetization that is peaked at the substrate-film interface (surface).

inverse fast Fourier transformation (FFT) of just the (110) diffraction spots of both film and substrate. The resulting image of the (110) lattice planes [Fig. 1(e)] shows regions of both continuous and discontinuous contrast at the direct interface, respectively indicating the coherent strain of film lattice planes with respect to the substrate [inset, Fig. 1(e)] and the presence of local structural incoherence and crystal defects. Figures 1(f) and 1(g) show close views of interfacial regions where disorder is clearly evident. In Fig. 1(f) the incoherent alignment of the film and substrate lattices result in an extra (110) plane on the film side. In Fig. 1(g) a misfit dislocation characterized by an extra (110) plane on the substrate side is observed at the direct interface. In these selected regions, dislocations are visible both at the direct interface and randomly distributed within the explored ≈ 10 nm thick volume (marked by ovals). The presence of defects in such a volume is consistent with the reduced channeling observed by the c-RBS measurements. Overall, our study of the LMO-YAO interface region shows how the lattice mismatch is accommodated at the expense of film crystallinity by both strain and misfit dislocations. Thus, the LMO-YAO interface can be categorized as only semicoherent.

Next we discuss the FM properties of the LMO thin films. Ferromagnetism in a 56 nm thick film is noted by standard bulk measurements of the $M(H)$ hysteresis loops at 5 K, with $\mu_0 H \parallel (001)$ [Figs. 2(a) and 2(b)]. Figure 2(a) shows the zero field-cooled $M(H)$ loop to reach a

maximum by 3 T and to give an average magnetization across the film of $\langle \mu_{Mn} \rangle = 0.49(1)\mu_B$. The detailed FM magnetization profile perpendicular to the LMO-YAO interface was studied by polarized neutron reflectometry (PNR) using the time-of-flight neutron reflectometer AMOR at PSI [23]. The momentum transfer-dependent reflectivity $R(q_z)$ probes the depth profile of both the chemical composition and the magnetic induction, since both determine the neutron index of refraction. The sensitivity to the in-plane magnetic induction is revealed by differences in the reflectivity curves for neutrons of opposite polarizations [neutron spin parallel (+) and antiparallel (-) to the external field] at the same q_z value.

Figure 2(c) shows reflectivity curves obtained from an ≈ 56 nm thick LMO film, for both spin directions at $T = 150$ K and $T = 10$ K and for $\mu_0 H \parallel (001) = 4$ T. The dominant contribution to the reflectivity is the chemical composition: the average film density determines the total external reflection up to $q_z = 0.016 \text{ \AA}^{-1}$. The interference of the neutrons reflected from both the surface and the LMO-YAO interface leads to the fringes visible at higher q_z . The frequency of this oscillation gives the expected film thickness of $t \approx 56$ nm. At 150 K, $R(q_z)$ for both spin directions are equal. On cooling, a difference between spin up and down is first detected at ≈ 100 K and is largest at the lowest measured T of 10 K. For clarity, in Fig. 2(d) we present the normalized ratio $(R^+ - R^-)/0.5(R^+ + R^-)$ for the 10 K measurement.

To analyze the PNR measurements quantitatively, the internal magnetization distribution was modeled by the following Gaussian profile: $\mu_{Mn}(z) = 1.07\mu_B \exp[-(z/39 \text{ nm})^2]$, with the peak at $z = 0$ located at the interface. Using this profile, Fig. 2(d) shows excellent agreement between the simulation (red line) and the experimental data. In comparison, the simulation with the same Gaussian function centered at the film surface (black line) clearly contradicts the data. Other model functions, such as a gauss error function, were tried for the simulation. While the precise details of the moment decay are model dependent, the essential details of the magnetization distribution were captured by all model functions: a FM interface layer typically ≈ 10 nm thick with $\mu_{Mn} \approx 1.1\mu_B$, and the moment decaying towards the film surface. According to the Gaussian profile, 50% of the integrated magnetization exists within the first 18 nm of the film, and the average moment per Mn of $\langle \mu_{Mn} \rangle \approx 0.50(5)\mu_B$ agrees well with the bulk $M(H)$ measurements.

Next we discuss how the established ferromagnetism coexists with AFM order in the films. By comparing between the zero field-cooled $M(H)$ loop (black curve) and a loop measured after field cooling in 4 T [red curve in Fig. 2(b)], a significant shift of 205 Oe in the field-cooled loop is noted and signals a clear exchange bias between the ferromagnetism and the expected AFM fraction in the sample. This exchange field establishes the

coupling between two magnetic phases in our LMO thin films, which is an attractive property for applications.

The antiferromagnetism in an ≈ 80 nm thick LMO film was studied by neutron diffraction using the RITA-II instrument at PSI, and the D10 instrument at ILL, France [23]. The observation of magnetic Bragg peaks [Fig. 3(a)] is due to the long-range AFM order of Mn spins. The T dependence of these peaks indicates the AFM magnetic transition to be ≈ 40 K [Fig. 3(b)]. The magnetic peaks are located at $\mathbf{G} \pm \mathbf{q}$, where \mathbf{G} is a reciprocal lattice vector, and $\mathbf{q} = (0q_k0)$ is the magnetic wave vector in reciprocal lattice units. Measurements of the $(0q_k1)$ peak evidence incommensurate (IC) magnetic order in the film with $q_k = 0.482(3)$ [Fig. 3(a)]. This signals a remarkable change in both the magnetic symmetry and the AFM order compared with the commensurate E -type order seen in bulk o-LMO with $q_k = 0.5$ [20]. The magnetic incommensuration in the film is confirmed by the observation of a weak peak located at $(01-q_k1)$, and five further IC peaks. A full magnetic structure refinement is not possible from the data, though the intensity distribution of the six peaks allows for a feasible \mathbf{bc} cycloid. This proposal is consistent with measurements of the $(0q_k1)$ peak with the film under $\mu_0 H \parallel \mathbf{a}$ [Fig. 3(c)], which evidence neither a spin flop transition nor a change in magnetic symmetry for fields up to 10 T.

The differences between the lattice constants of the films and bulk LMO indicate strain to exist throughout the coherent volume of the film. Therefore, our neutron diffraction results evidence a strain-induced change of the AFM structure in the films compared with the bulk. Without large strain-induced changes in the (T -dependent) electronic structure [25], the change in the AFM structure seen in the films likely reflects a strain-induced alteration of the magnetic interactions or the Mn orbital order. According to both calculations [27] and the magnetic phase diagram reported by Goto *et al.* [28], a small increase in the Mn-O-Mn bond angle would shift the magnetism away from the E type and towards a cycloidal spin structure. Other theoretical work shows IC spiral and E -type states in bulk REMnO_3 may display very similar free energies [29]. This could explain the observations in YMnO_3 where a mixed phase of E type and cycloidal AFM orders was measured by Wadati *et al.* [30] and indirectly concluded to be a spiral phase by Fina *et al.* [31]. Therefore, we expect that a strain-induced alteration of the magnetic interactions is pivotal in determining the IC magnetic ground state in the LMO thin films. Another influence of the film strain is shown in Fig. 3(a) where it is seen that the width of the AFM peak is not resolution limited. The resolution-corrected magnetic correlation length is $17(3)$ nm and so significantly shorter than the effective film thickness of 66 nm along the direction of \mathbf{q} .

In Fig. 3(d), we sketch the expected magnetic situation in the LMO thin films. The FM magnetization displays, e.g., a Gaussian profile that is peaked at the interface and

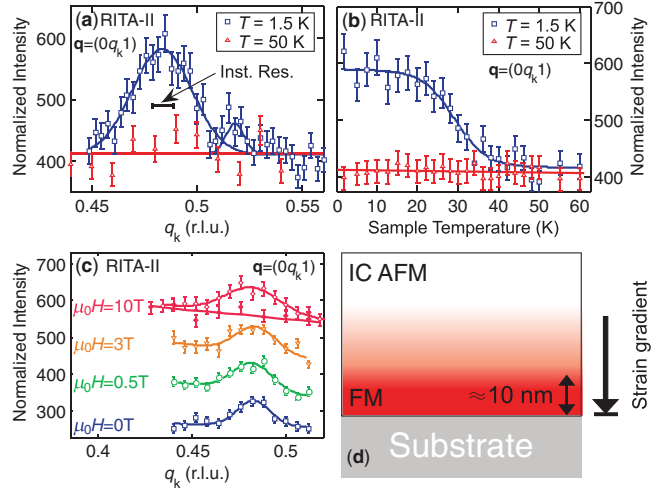


FIG. 3 (color online). (a) The $(0q_k1)$ AFM peak in a LuMnO_3 thin film. A Gaussian fit of the main peak gives the peak center at $q_k = 0.482(3)$. The solid bar indicates the instrumental resolution of RITA-II. (b) The T dependence of the $(0q_k1)$ peak, with lines as guides for the eye. (c) The $\mu_0 H$ dependence of $(0q_k1)$ for $\mu_0 H \parallel \mathbf{a}$ up to 10 T. Empty (filled) symbols denote data taken $T = 2$ K ($T = 50$ K). Curves are displaced vertically for clarity and peaks are fitted with Gaussian line shapes. (d) Sketch to illustrate the magnetic situation in the LMO film. The FM layer located near the strained film-substrate interface evolves towards a likely cycloidal IC AFM order when moving down the strain gradient towards the film surface.

which is much reduced at the film surface. On moving away from the interface region, the magnetism evolves towards long-range, likely cycloidal, incommensurate AFM order. Here we note that since the precise deviation of the AFM order away from the E type is sensitive to the film strain, it may be expected that the E type is present, or even dominant, with increasingly thicker films. Consequently, a single sample may simultaneously host different magnetic structures. The illustration of the single phase material shown in Fig. 3(d) is equivalent to an artificial structure described in Ref. [32] and realized experimentally in Ref. [33].

A FM magnetization distribution that is peaked at the LMO-YAO interface strongly excludes that it originates from within crystal domain boundaries, since few are to be expected in our twin-free films. Note that this is unlike REMnO_3 thin films grown on (100) SrTiO_3 and in which a uniform magnetization distribution across the film was identified using PNR [34]. Instead, the FM magnetization in the LMO films is peaked where the strain gradient is largest and where the film hosts regions of epitaxially strained lattice planes with monoclinic distortion [24] and strain-induced crystal defects. On moving away from the interface, the decay of the FM magnetization is concomitant with the shallowing lattice strain gradient. All of these observations tie the origin of the FM magnetization strongly to strain-induced alterations of the crystal

properties which are most pronounced close to the interface. Nevertheless, the microscopic origin of the strain-induced ferromagnetism remains to be addressed since the conversion between AFM and FM ground states within one material cannot be explained easily. One possibility is that the monoclinic distortion of the orthorhombic lattice, which is also largest at the interface [24], could provide the necessary reduction of crystal symmetry that alters the orbital ordering and allows a uniform magnetization to be manifested independently of the bulk AFM order. Alternatively, the strain-induced misfit dislocations may locally host small variations in stoichiometry that display FM properties. These proposals can be tested by XMCD experiments.

Our experimental results could also be explained by a strain-induced change in the relative strength of the exchange interactions. However, since none of the bulk materials show macroscopic moment FM phases, and the exchange along the c axis is solidly AFM, we think that such a scenario is unlikely. Further, this proposal would also not explain why similar FM properties have been observed for various REMnO_3 films grown on a range of different substrates [18,34]. An alternative possibility is that the growth-induced strain causes a canting of the AFM phase below T_N , and so, a projection of the FM moment is observed. This could explain the reduced Mn moment of $\approx 1\mu_B$ at the interface. However, the FM moment is first detected by PNR well above T_N at ≈ 100 K. Moreover, the measured exchange field does not support spin canting as the origin for the observed FM signal.

To summarize, we have shown unequivocally that LuMnO_3 thin films grown on YAlO_3 substrates display a large moment ($\approx 1\mu_B$) ferromagnetic magnetization that is peaked at the highly strained substrate-film interface. We demonstrated the direct coupling between the ferromagnetism and the antiferromagnetic order also present in the same phase below ≈ 40 K. Our approach comprised a novel route for generating coupled magnetic orders in a single phase thin film. Such effects should also be present at room temperature and our study paves the way for the development of new multifunction devices.

Work at the PSI is supported via both the SNF and the NCCR program MaNEP. Neutron experiments were performed at the Swiss Spallation Neutron Source, SINQ, PSI,

Switzerland and at the ILL, France. We acknowledge support by the Electron Microscopy Center of ETH Zürich (EMEZ) and thank Ch. Bernhard, M. Fiebig, J. Fontcuberta, and M. Laver for valuable discussions.

*christof.schneider@psi.ch

- [1] H. Y. Hwang *et al.*, *Nat. Mater.* **11**, 103 (2012).
- [2] A. Ohtomo *et al.*, *Nature (London)* **419**, 378 (2002).
- [3] A. Ohtomo and H. Y. Hwang, *Nature (London)* **427**, 423 (2004).
- [4] N. Reyren *et al.*, *Science* **317**, 1196 (2007).
- [5] S. Dong *et al.*, *Phys. Rev. B* **78**, 201102 (2008).
- [6] N. Kida *et al.*, *Phys. Rev. Lett.* **99**, 197404 (2007).
- [7] C. Adamo *et al.*, *Appl. Phys. Lett.* **92**, 112508 (2008).
- [8] J. Seidel *et al.*, *Nat. Mater.* **8**, 229 (2009).
- [9] A. Y. Emelyanov *et al.*, *J. Appl. Phys.* **89**, 1355 (2001).
- [10] M. M. Saad *et al.*, *J. Phys. Condens. Matter* **16**, L451 (2004).
- [11] N. A. Hill, *J. Phys. Chem. B* **104**, 6694 (2000).
- [12] S.-W. Cheong and M. Mostovoy, *Nat. Mater.* **6**, 13 (2007).
- [13] T. Kimura *et al.*, *Nature (London)* **426**, 55 (2003).
- [14] M. Kenzelmann *et al.*, *Phys. Rev. Lett.* **95**, 087206 (2005).
- [15] I. Fina *et al.*, *Appl. Phys. Lett.* **97**, 232905 (2010).
- [16] D. Rubi *et al.*, *Phys. Rev. B* **79**, 014416 (2009).
- [17] C. J. M. Daumont *et al.*, *J. Phys. Condens. Matter* **21**, 182001 (2009).
- [18] X. Marti *et al.*, *J. Appl. Phys.* **108**, 123917 (2010).
- [19] M. Garganourakis *et al.*, *Phys. Rev. B* **86**, 054425 (2012).
- [20] H. Okamoto *et al.*, *Solid State Commun.* **146**, 152 (2008).
- [21] V. Pomjakushin *et al.* (unpublished).
- [22] Substrates from CrysTec GmbH, Berlin, Germany.
- [23] See Supplemental Material at <http://link.aps.org/supplemental/10.1103/PhysRevLett.111.037201> for further details.
- [24] Y. Hu *et al.*, *Appl. Surf. Sci.* **258**, 9323 (2012); Y. Hu *et al.*, *ibid.* **278**, 92 (2013); Y. Hu, Ph.D. thesis, ETH Zürich, 2013.
- [25] Y. Hu *et al.*, *Appl. Phys. Lett.* **100**, 252901 (2012).
- [26] M. Döbeli, *J. Phys. Condens. Matter* **20**, 264010 (2008).
- [27] S. Dong *et al.*, *Phys. Rev. B* **78**, 155121 (2008).
- [28] T. Goto *et al.*, *Phys. Rev. Lett.* **92**, 257201 (2004).
- [29] M. Mochizuki *et al.*, *Phys. Rev. B* **84**, 144409 (2011).
- [30] H. Wadati *et al.*, *Phys. Rev. Lett.* **108**, 047203 (2012).
- [31] I. Fina *et al.*, *Phys. Rev. Lett.* **107**, 257601 (2011).
- [32] R. Ramesh and N. A. Spaldin, *Nat. Mater.* **6**, 21 (2007).
- [33] Y.-H. Chu *et al.*, *Nat. Mater.* **7**, 478 (2008).
- [34] B. J. Kirby *et al.*, *J. Appl. Phys.* **105**, 07D917 (2009).